RNA (2002), *8*:307–323. Cambridge University Press. Printed in the USA.

DOI: 10.1017.S1355838202024226

Effects of magnesium ions on the stabilization of RNA oligomers of defined structures

MARTIN J. SERRA,[1] JOHN D. BAIRD,[1] TARAKA DALE,[1] BRIDGET L. FEY,[1] KIMBERLY RETATAGOS,[1] and ERIC WESTHOF[2]

[1]Department of Chemistry, Allegheny College, Meadville, Pennsylvania 16335, USA
[2]Institut de Biologie Moléculaire et Cellulaire du Centre National de la Recherche Scientifique, Modélisations and Simulations des Acides Nucléiques, Unité Propre de Recherche 9002, F-67084 Strasbourg Cedex, France

ABSTRACT

Optical melting was used to determine the stabilities of 11 small RNA oligomers of defined secondary structure as a function of magnesium ion concentration. The oligomers included helices composed of Watson–Crick base pairs, GA tandem base pairs, GU tandem base pairs, and loop E motifs (both eubacterial and eukaryotic). The effect of magnesium ion concentration on stability was interpreted in terms of two simple models. The first assumes an uptake of metal ion upon duplex formation. The second assumes nonspecific electrostatic attraction of metal ions to the RNA oligomer. For all oligomers, except the eubacterial loop E, the data could best be interpreted as nonspecific binding of metal ions to the RNAs. The effect of magnesium ions on the stability of the eubacterial loop E was distinct from that seen with the other oligomers in two ways. First, the extent of stabilization by magnesium ions (as measured by either change in melting temperature or free energy) was three times greater than that observed for the other helical oligomers. Second, the presence of magnesium ions produces a doubling of the enthalpy for the melting transition. These results indicate that magnesium ion stabilizes the eubacterial loop E sequence by chelating the RNA specifically. Further, these results on a rather small system shed light on the large enthalpy changes observed upon thermal unfolding of large RNAs like group I introns. It is suggested that parts of those large enthalpy changes observed in the folding of RNAs may be assigned to variations in the hydration states and types of coordinating atoms in some specifically bound magnesium ions and to an increase in the observed cooperativity of the folding transition due to the binding of those magnesium ions coupling the two stems together. Brownian dynamic simulations, carried out to visualize the metal ion binding sites, reveal rather delocalized ionic densities in all oligomers, except for the eubacterial loop E, in which precisely located ion densities were previously calculated.

Keywords: Brownian dynamics; magnesium stabilization; RNA oligomers; thermal stability

INTRODUCTION

The polyanionic nature of RNA requires compensating charges for the formation of stably folded structures because of the electrostatic repulsion of closely packed backbone phosphates. Cations play a critical role in reducing the repulsion and facilitating the folding of RNAs into their structurally active forms. Both monovalent and divalent ions can stabilize nucleic acid structure by nonspecific interaction with the anionic backbone. Divalent ions, particularly Mg^{2+} ions, have been shown to have unique, but controversial, roles in nucleic acid stabilization (Brion & Westhof, 1997; Misra & Draper, 1999a). The unique ability of divalent metal ions, particularly Mg^{2+} to stabilize nucleic acids has been observed for both DNAs (Record, 1975) and large RNAs, such as tRNAs (Cole et al., 1972). The tertiary structure of ribozymes have been shown to be stabilized by Mg^{2+} ions even in the presence of high concentrations of monovalent ions (Pyle, 1993). The role of metal ions on RNA structural stability and function has recently been reviewed (Fieg & Uhlenbeck, 1999; Misra & Draper, 1999a).

Much of what is known about the interaction of metal ions with nucleic acids, in particular Mg^{2+} ions, has come from the study of polymeric nucleic acids. DNA, poly(A), poly(U), or poly(AU) are stabilized by a highly delocalized cloud of metal ions (Porschke, 1973). The nonspecific interaction of metal ions with these polymeric molecules can be modeled by treating the nu-

Reprint requests to: Eric Westhof, Institut de Biologie Moléculaire et Cellulaire du CNRS Modélisations and Simulations des Acides Nucléiques UPR 9002, 15 rue René Descartes, F-67084 Strasbourg Cedex, France; e-mail: E.Westhof@ibmc.u-strasbg.fr.

cleic acid as an infinitely long rigid rod of uniform charge density using counterion condensation theory (Manning, 1977; Anderson & Record, 1995) and nonlinear Poisson–Boltzmann theory (Sharp et al., 1995; Hermann & Westhof, 1998; Misra & Draper, 1999b, 2000).

In contrast, little is known about the interaction of metal ions with oligonucleotides where end and sequence effects may be important determinates. The structures of large RNAs have been shown to involve the packing of helical domains, sometimes mediated by metal ion contacts (Batey et al., 1999). Because ions are hydrated in aqueous solutions, the binding modes have been classified as outer-sphere when the ion binds to the RNA with its complete primary hydration shell or inner-sphere when partial or full ion dehydration occurs (Porschke, 1973). In the former case, the RNA and the ion share water of hydration whereas, in the latter case, energetically unfavorable dehydration of both the ion and the RNA must occur. Thus, metal ions can stabilize RNA structures in two ways (Laing et al., 1994). First, the metal ions can bind in a "nonspecific" manner by delocalized Coulombic neutralization of the phosphate backbone mainly via outer-sphere binding (however, in some instances, outer-sphere binding could also be viewed as "specific"). Second, inner-sphere binding of partially dehydrated metal ions dock into specific "binding pockets" where the chemical nature of the cation and the atomic types lining the RNA binding pocket play organizing and ordering roles. Although X-ray structures display both types of ion binding, the recent high-resolution tRNA structures (Jovine et al., 2000; Shi & Moore, 2000) containing magnesium ions indicate clearly that outer-sphere binding is prevalent and that only one, and at most two, magnesium ions bind as inner-sphere with direct contact(s) to the RNA (i.e., with one (two) molecule(s) of water of hydration displaced).

UV-melting experiments performed on large RNAs, like group I introns (Banerjee et al., 1993; Tanner & Cech, 1996; Brion et al., 1999), show a large apparent enthalpic change associated with the tertiary structure thermal unfolding that increases strongly with increasing concentrations of divalent ions, especially magnesium ions. With large RNAs, it is difficult to assess the origins of such complex effects because of, among other factors, the large number of "nonspecific" ions interacting with the RNA. Therefore, we selected a number of small RNA oligomers of defined structure to investigate the interactions of Mg^{2+} ions using optical melting experiments. The three duplexes composed entirely of Watson–Crick base pairs provide a regular repetitive structure (A-form geometry) for comparison. The structural geometry of each of the tandem GA and GU pairs provides ligand atoms, base O or N atoms, in unique orientation for the formation of metal ion complexes. Several of these RNAs (tandem GU and the non-Watson–Crick pairs of loop E) have metal ions associated with them in crystal (Cate & Doudna, 1996; Correll et al., 1997). Brownian-dynamic (BD) simulations were also conducted to visualize the interaction of magnesium ions, modeled as charged (+2) spheres of radii 1.2–2.2 Å, corresponding roughly to a dehydrated and a fully hydrated ion, with the RNA oligomers (Hermann & Westhof, 1998). Trajectories are calculated by simulating Brownian motion and the electrostatic field generated by the RNA as calculated in the non-Poisson–Boltzmann approximation (Madura et al., 1994).

RESULTS

Optical melting experiments of RNA oligomers are usually performed in 1.0 M monovalent ion (Na^+) conditions to compensate for the absence of divalent ions. To investigate the role of Mg^{2+} ions on the stability of RNA oligomers, the concentration of monovalent ions in these optical melting experiments was set to a more physiological concentration of 0.1 M NaCl (Table 1). In all cases, there was good agreement between the thermodynamic values derived from the T_M^{-1} versus log C_t plots and the melt curves (see Materials and Methods). As expected, all of the oligomers were more stable in 1.0 M NaCl than in 0.1 M NaCl melt buffer (Table 1); the hexamer duplex has a higher melting temperature by 7.7 °C, the octamer duplex by 10.5 °C and the 14mer by 13.4 °C. The changes in melting temperature for the RNA oligomers are summarized in Table 2. The differences in melting temperatures between 1.0 M and 0.1 M melt buffer were 8–10 °C for oligomers with tandem GA base pairs and about 9–10 °C for oligomer duplexes with tandem GU base pairs. Thus, both the GA and GU sequences present changes in melting temperatures similar to those of duplexes of comparable length. The introduction of non-Watson–Crick pairs within a duplex seems to have minimal effects on the relative stabilities of the oligomers in melt buffer containing only monovalent ions. The largest oligomer investigated, containing the eubacterial loop E motif flanked by Watson–Crick pairs (13 nt), had the largest change in melting temperature (almost 23 °C). The other oligomers with the loop E motifs (loop E hairpin and eukaryotic) have only modest temperature changes: 8–9 °C.

The three duplex sequences were then melted in 0.1 M NaCl melt buffer with a series of magnesium ion concentrations up to 50 mM. The thermodynamics for duplex formation by the oligomers in 50 mM $MgCl_2$, 0.1 M NaCl melt buffer is presented in Table 1; all of the duplexes are more stable in buffer containing Mg^{2+} ion. The melting temperature of hexamer duplex increases by 12.1 °C, the octamer duplex increases by 11.2 °C, and the 14mer duplex increases by 11.0 °C. As opposed to the stability increases in monovalent ions, the stability increases observed with magnesium ion are inversely related to the size of the oligomer (Table 2).

TABLE 1. Thermodynamic parameters for duplex formation.[a]

	T_M^{-1} vs. log C_t plots				Average of curve fits			
Oligomers	$-\Delta H^\circ$ (kcal/mol)	$-\Delta S^\circ$ (eu)	$-\Delta G^\circ_{37}$ (kcal/mol)	T_M[b] (°C)	$-\Delta H^\circ$ (kcal/mol)	$-\Delta S^\circ$ (eu)	$-\Delta G^\circ_{37}$ (kcal/mol)	T_M[b] (°C)
Duplex								
CCAUGG	51.5	147.0	6.0	38.8	58.5	169.4	6.0	38.6
GGUACC	56.7[c]	157.0	7.3	46.3	61.9	175.3	7.5	46.4
	56.9	157.1	8.1	51.0	60.9	169.7	8.3	50.7
CCAUAUGG	64.2	183.1	7.4	45.7	70.4	202.3	7.6	45.8
GGUAUACC					70.6[d]	196.0	9.7	56.3
	79.2	221.5	10.5	57.0	80.9	226.8	10.6	57.0
CCUUGAUAUCAAGG	116.8	330.0	14.4	62.1	103.5	288.0	14.2	64.8
GGAACUAUAGUUCC	96.6	257.4	16.8	77.2	102.4	274.6	17.2	76.4
	97.9	263.6	16.1	74.1	91.2	244.1	15.6	74.6
Tandem GA								
GGC**GA**GCC	56.0	155.6	7.7	47.1	59.9	168.6	7.6	47.3
CCG**AG**CGG	66.1[e]	181.8	9.7	57.0	73.9	205.6	10.2	57.0
	71.8	197.8	10.4	58.9	70.8	194.6	10.4	59.1
GGC**AG**GCC	69.5	199.4	7.6	46.1	69.6	199.6	7.7	46.2
CCG**GA**CGG	69.0	192.9	9.2	53.7	70.8	198.2	9.3	53.8
	76.3	213.9	9.9	55.3	64.9	178.9	9.4	56.0
Tandem GU								
GCA**UG**UGC	66.1	193.6	6.0	38.6	67.3	197.3	6.1	38.9
CGU**GU**ACG	72.4	206.1	8.4	49.2	73.0	208.0	8.5	49.4
	58.5	163.8	7.7	48.1	57.2	160.0	7.9	49.5
GCA**GU**UGC	40.8	116.8	4.6	29.1	46.9	137.0	4.4	29.0
CGU**UG**ACG	64.8	190.0	5.9	38.1	69.3	203.9	6.0	38.6
	48.2	135.4	6.2	40.1	56.3	160.9	6.4	41.0
GCU**GG**UGC	55.8	161.0	5.8	33.2	56.1	162.0	5.8	33.2
CGA**UU**ACG	69.4	199.1	7.6	42.0	71.8	206.6	7.7	42.1
	67.8	193.5	7.8	42.9	74.2	214.0	7.9	42.7
Loop E motifs								
GCG**AGUA**GGC	45.5	125.8	6.5	36.9	48.6	135.2	6.7	38.1
CGC**A AG**CCG	47.8	128.4	8.0	46.8	56.2	154.7	8.2	45.4
	54.4	145.7	9.2	53.3	60.3	162.5	9.9	54.2
Loop E hairpin[f]					31.8	96.8	1.8	55.5
					54.1	160.9	4.2	63.0
GCC**GAUGGUA**GCC	41.0	116.5	4.9	25.1	43.0	123.3	4.8	24.9
CGG**AUGAGAG**CGG	66.2	185.6	8.7	47.3	66.2	185.2	8.8	47.9
	98.6[g]	273.8	13.7	61.4	98.7	270.8	13.7	61.6

[a] Solutions are: top line: 0.1 M NaCl, 10 mM sodium cacodylate, 0.5 mM EDTA, pH 7; middle line: 1.0 M NaCl, 0.5 mM EDTA, 10 mM sodium cacodylate, pH 7; and bottom line: 50 mM $MgCl_2$, 0.1 M NaCl, 10 mM sodium cacodylate, pH 7.

[b] Calculated at 10^{-4} M oligomer concentration. Estimated errors in ΔG°_{37}, ΔH°, and ΔS° are 2%, 10%, 10%, respectively.

[c] McDowell et al. (1997).

[d] Predicted (Xia et al., 1998).

[e] SantaLucia et al. (1990).

[f] 5′-GCC**GAUGGUA**GC^{G}U
CGG**AUGAGAG**CG$_{A}$A

[g] 20 mM $MgCl_2$, 0.1 M NaCl, 10 mM sodium cacodylate, pH7.

Except for the 14 mer, the melting temperature of the duplex sequences in the 50 mM Mg^{2+} buffer are larger than those observed in the 1.0 M NaCl melt buffer despite the fact that the magnesium buffer has only half the ionic strength of the 1.0 M NaCl buffer. In general, the van't Hoff enthalpy increases slightly with the addition of magnesium ion. However, the 14mer actually presents a slight decrease in the van't Hoff enthalpy in the 50 mM magnesium ion melt buffer relative to the 0.1 M NaCl melt buffer without magnesium ion (Table 1). Figures 1A,B display the changes in melting temperature of the duplexes with increasing magnesium ion concentration. The results seen here for the RNA oligomers are similar to those observed previously for a DNA duplex (5′d(GCATGC)$_2$; Williams et al., 1989) indicating that similar interactions occur with magnesium ions and both DNA and RNA oligomers.

TABLE 2. Summary of melting temperature and free energy changes at different Na^+ and Mg^{2+} concentrations.

Oligomer	ΔT_M (1.0–0.1 Na)[a]	$\Delta\Delta G_{37}$ (1.0–0.1 Na)[b]	ΔT_M (50–0 Mg)[c]	$\Delta\Delta G_{37}$ (50–0 Mg)[d]	$\frac{\Delta T_{M(50-0Mg)}}{\Delta_{M(1.0-0.1Na)}}$[e]	$\frac{\Delta\Delta G_{37\ (50-0\ Mg)}}{\Delta\Delta G_{37\ (1.0-0.1\ Na)}}$[f]
CCAUGG GGUACC	7.7	1.4	12.1	2.2	1.6	1.6
CCAUAUGG GGUAUACC	10.5	2.2	11.2	3.1	1.1	1.4
CCUUGAUAUCAAGG GGAACUAUAGUUCC	13.4	2.7	11.0	1.5	0.8	0.6
GGC**GA**GCC CCG**AG**CGG	9.8	2.4	11.8	2.8	1.2	1.2
GGC**AG**GCC CCG**GA**CGG	7.6	1.6	9.4	2.0	1.2	1.2
GCA**UG**UGC CGU**GU**ACG	10.5	2.4	10.0	1.8	1.0	0.8
GCA**GU**UGC CGU**UG**ACG	9.4	1.5	11.6	1.8	1.2	1.2
GCU**GG**UGC CGA**UU**ACG	8.8	1.8	9.6	2.0	1.1	1.1
GCG**AGUA**GGC CGC**A AG**CCG	8.6	1.5	16.3	3.0	1.9	2.0
Loop E hairpin[g]	7.5	2.4				
GCC**GAUGGUA**GCC CGG**AUGAGAG**CGG	22.6	3.9	36.5[h]	8.9[h]	1.6	2.3

[a]Difference in melting temperature for the oligomer in 1.0 M NaCl, 10 mM cacodylate, pH 7.0, and 0.1 M NaCl, 10 mM cacodylate, pH 7.0, calculated at 10^{-4} M oligomer concentration.
[b]Difference in ΔG_{37} for the oligomer in 1.0 M NaCl, 10 mM cacodylate, pH 7.0, and 0.1 M NaCl, 10 mM cacodylate, pH 7.0.
[c]Difference in melting temperature for the oligomer in 50 mM $MgCl_2$, 0.1 M NaCl, 10 mM cacodylate, pH 7.0, and 0.1 M NaCl, 10 mM cacodylate, pH 7.0, calculated at 10^{-4} M oligomer concentration.
[d]Difference in ΔG_{37} for the oligomer in 50 mM $MgCl_2$, 0.1 M NaCl, 10 mM cacodylate, pH 7.0, and 0.1 M NaCl, 10 mM cacodylate, pH 7.0.
[e]Ratio of a and c.
[f]Ratio of b and d.
[g]5′-GCC**GAUGGUA**GC^{G}U
CGG**AUGAGAG**CG$_{A}$A
[h]Values are for 20 mM $MgCl_2$.

The effect of magnesium ion on the thermal stability of the oligomers can be interpreted using either of two simple models (Laing et al., 1994). The first one assumes that the larger stability can be viewed as an increase in the number of metal ions bound to the duplex relative to the single-stranded form. The graph of $1/T_M$ versus $\ln[Mg^{2+}]$ should be a straight line with the slope related to Δn, the change in number of ions bound (see equation 1). Here, $1/T_M$ is the reciprocal melting temperature in Kelvin, R is the gas constant, and ΔH is the enthalpy for the formation of duplex.

$$\frac{d(1/T_M)}{d\ln([Mg])} = -\left(\frac{R}{\Delta H}\right)\Delta n. \quad (1)$$

Figure 1C displays the graph of $1/T_M$ versus $\ln[Mg^{2+}]$ for the three duplex oligomers. The results are summarized in Table 3 and indicate that less than one additional Mg^{2+} ion binds to the duplexes relative to the single strands. Δn is often expressed as the change in metal ions bound per base pair, in which case Δn would be less than 0.1 per base pair. Interestingly, the Δn values are inversely related to the length of the oligomer. The value of Δn can approach 0.5 per base pair for polymeric nucleic acids when measured in the presence of much lower monovalent ion concentration (0.01 M; Record, 1975).

The second model assumes that the same number of ions is bound to the duplex and single-stranded forms (where the number of Mg^{2+} ions is assumed to be equal to half the number of phosphates in the RNA) but that the affinity of the metal ion for the duplex is greater (see equation 2; Laing et al., 1994). Here, R is the gas constant, m is the number of phosphates in the duplex, ΔH is the enthalpy for duplex formation, K_f and K_u are the binding constants for magnesium ion to the duplex and single-stranded forms of the oligomer, and $1/T_{M_0}$ is the reciprocal

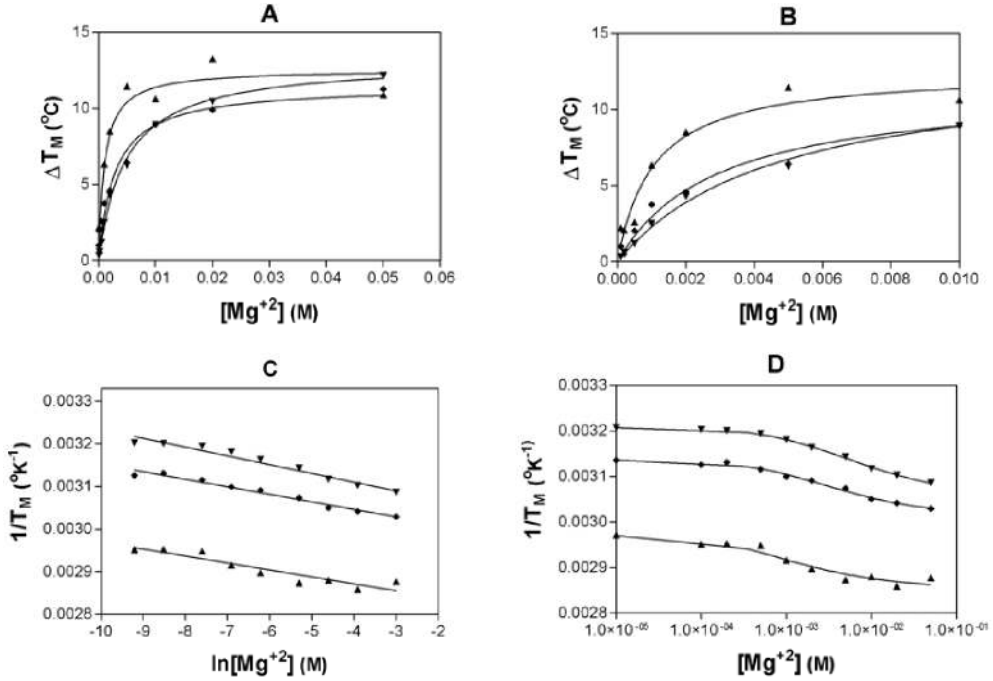

FIGURE 1. Stabilization of RNA oligomers with Watson–Crick base pairs by Mg^{2+}. **A,B:** Change in melting temperature (at 1×10^{-4} M oligomer) as a function of [Mg^{2+}], high (**A**) and low (**B**) magnesium concentrations. **C**: Reciprocal T_M plotted as a function of added Mg^{2+}. The lines are the least squares fit of the data to equation 1. **D**: Reciprocal T_M plotted as a function of added Mg^{2+} (x axis is ln scale). The curves are the least squares fit of the data to equation 2. The T_M value at 10^{-5} M is the reciprocal melting temperature in the absence of Mg^{2+} and is not used in the fit.▼: $(5'CCAUGG)_2$, ●: $(5'CCAUAUGG)_2$, ▲: $(5'CCUUGAUAUCAAGG)_2$.

melting temperature (in Kelvin) in the absence of magnesium ion.

$$\frac{1}{T_M} = \left(\left(\frac{R \cdot m/2)}{\Delta H}\right) \cdot \ln\left(\frac{(\sqrt{1 + 4K_f \cdot [\mathrm{Mg}]}) + 1}{(\sqrt{1 + 4K_u \cdot [\mathrm{Mg}]}) + 1}\right)\right) + \frac{1}{T_{M_0}}. \quad (2)$$

This analysis produces a graph of $1/T_M$ versus ln[Mg^{2+}] that is sigmoidal. Figure 1D shows the $1/T_M$ versus ln[Mg^{2+}] data fitted to the second model. The data fit the sigmoidal curve better than the linear fit above. Therefore, it appears as though magnesium ions bind to the three duplexes in a nonspecific manner. The values for the Mg^{2+} binding constants are presented in Table 3. The binding constant to the single-stranded form of the hexamer RNAs is 40 M^{-1} whereas the binding constant to the ordered duplex is 260 M^{-1}. The binding constants to the octamer RNA are slightly higher: 92 M^{-1} for the single-stranded form and 370 M^{-1} for the duplex. The binding constants to the 14mer are much higher: 350 M^{-1} for the single-stranded form and 930 M^{-1} for the duplex. Figure 2 displays the direct relationship between size of the RNA oligomer and the magnesium ion binding constants to the duplex and single-stranded RNAs. As observed with the Δn values, there is an inverse relationship between the K_f/K_u ratio and the length of the oligomer (Table 3). A 1.5–2.0-fold increase in binding of Mg^{2+} ions to RNA hairpin structures was previously found (Laing et al., 1994). The Mg^{2+} binding constant for the ordered hairpins were 480 M^{-1} and 380 M^{-1} for a 59- and a 15-nt oligomer. The binding constant to the single-stranded RNAs were 260 M^{-1} and 270 M^{-1}, respectively. Previously measured Mg^{2+} binding constants to polymeric RNAs range from 180 M^{-1} (poly (U)) to 490 M^{-1} (poly(A)-poly(U); Record et al., 1976). The similarity in values determined here to those previously measured for the homopolymers argues further in favor of a nonspecific interpretation for the Mg^{2+} ion stabilization.

The structure of the hexamer $(5'CGUACdG)_2$, as solved by X-ray crystallography (Biswas & Sundaralingam, 1998), was used as a target in a series of BD simulations. The highest occupancy sites are located in the deep groove near the center of the duplex. The results are similar for either the 1.2 or 2.2 Å spheres (see Fig. 4). The lower occupancy sites, modeled as green polyhedra in the middle drawing and as space filling green spheres at the right of the figure, line the deep groove of the RNA.

Tandem GA base pairs belong to the commonly observed structural motifs in RNA. Ribosomal RNAs have

TABLE 3. Summary of values as derived from model 1 (Δn) and from model 2 (K_f, K_u) for Mg^{2+} ion binding.

Oligomer	Δn	Δn/base pair	K_f	K_u	K_f/K_u
CCAUGG GGUACC	0.61	0.10	260	40	6.5
CCAUAUGG GGUAUACC	0.67	0.08	370	92	4.0
CCUUGAUAUCAAGG GGAACUAUAGUUCC	0.90	0.06	930	350	2.6
GGC**GA**GCC CCG**AG**CGG	0.52	0.06	430	130	3.3
GGC**AG**GCC CCG**GA**CGG	0.40	0.05	260	84	3.1
GCA**UG**UGC CGU**GU**ACG	0.44	0.06	170	56	3.0
GCA**GU**UGC CGU**UG**ACG	0.54	0.07	91	25	3.6
GCU**GG**UGC CGA**UU**ACG	0.56	0.07	310	110	2.8
GCG**AGUA**GGC CGC**A AG**CCG	0.68	0.08	510	150	3.4
GCC**GAUGGUA**GCC CGG**AUGAGAG**CGG	2.1	0.15	2590	250	10.4
GCC**GAUGGUA**GCC[a] CGG**AUGAGAG**CGG	1.2			840(fixed)	310(fixed)
	40,000				

[a]Fit to model that combines specific and nonspecific binding; see text.

a marked preference for the sequence orientation 5′-GA/AG, which is, after the tandem of GU pairs, the most prevalent tandem of non-Watson–Crick pairs, whereas 5′-AG/GA is never observed (SantaLucia et al., 1990). To investigate the interaction of magnesium ions with non-Watson–Crick base pairs, we examined the effect of magnesium ion concentration on the thermal stability of two oligomers with tandem GA whose structures have been elucidated (SantaLucia & Turner, 1993; Wu & Turner, 1996). Depending upon sequence, tandem GA can form two types of pairs, either with a *cis* Watson–Crick/Watson–Crick configuration (imino), (5′GGC**AG**GCC)$_2$ or a *trans* Hoogsteen/sugar edge (sheared) conformation, (5′GGC**GA**GCC)$_2$ (Figs. 5 and 6; Leontis & Westhof, 2001). The AG non-Watson–Crick pairs in the sequence (5′GGC**AG**GCC)$_2$ form a structure with the helix underwound to favor intrastrand base stacking. To accommodate the *cis* Watson–Crick/Watson–Crick geometry, the deep groove is widened by about 5 Å relative to A-form geometry (Fig. 6; Wu & Turner, 1996). The GA non-Watson–Crick pairs in the sequence (5′GGC**GA**GCC)$_2$ form a structure with the helix overwound to favor interstrand base stacking. The geometry of the tandem *trans* Hoogsteen/sugar edge GA pairs causes a narrowing of the deep groove by about 4 Å relative to A-form geometry (Fig. 5; SantaLucia & Turner, 1993). In both sequences, the conformation of the GA base pairs present an arrangement of hydrophilic atoms in the deep groove that could serve as potential metal ion binding sites.

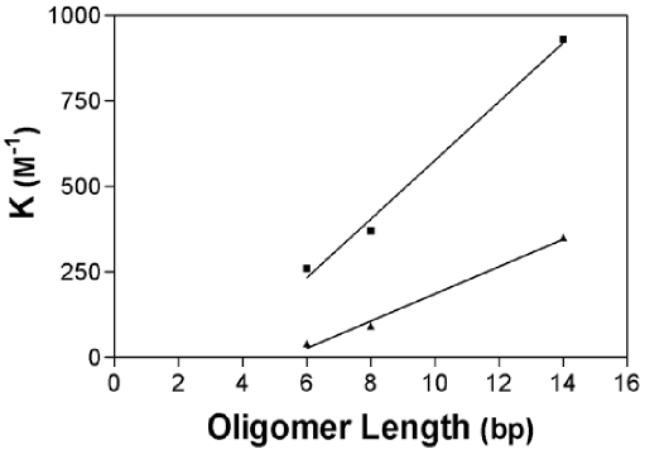

FIGURE 2. Effect of sequence length on the binding of magnesium ion. ▲: K_u, ■: K_f.

The energetic contribution (ΔG°_{37}), of the tandem GA pair in standard 1.0 M NaCl melt buffer is, as measured previously, −0.7 kcal/mol (SantaLucia et al., 1990). The thermodynamics of duplex formation for (5′GGC**AG**GCC)$_2$ in 1 M melt buffer has previously been measured (Xia et al., 1997). The thermodynamic values for (5′GGC**AG**GCC)$_2$ presented in Table 1 for duplex for-

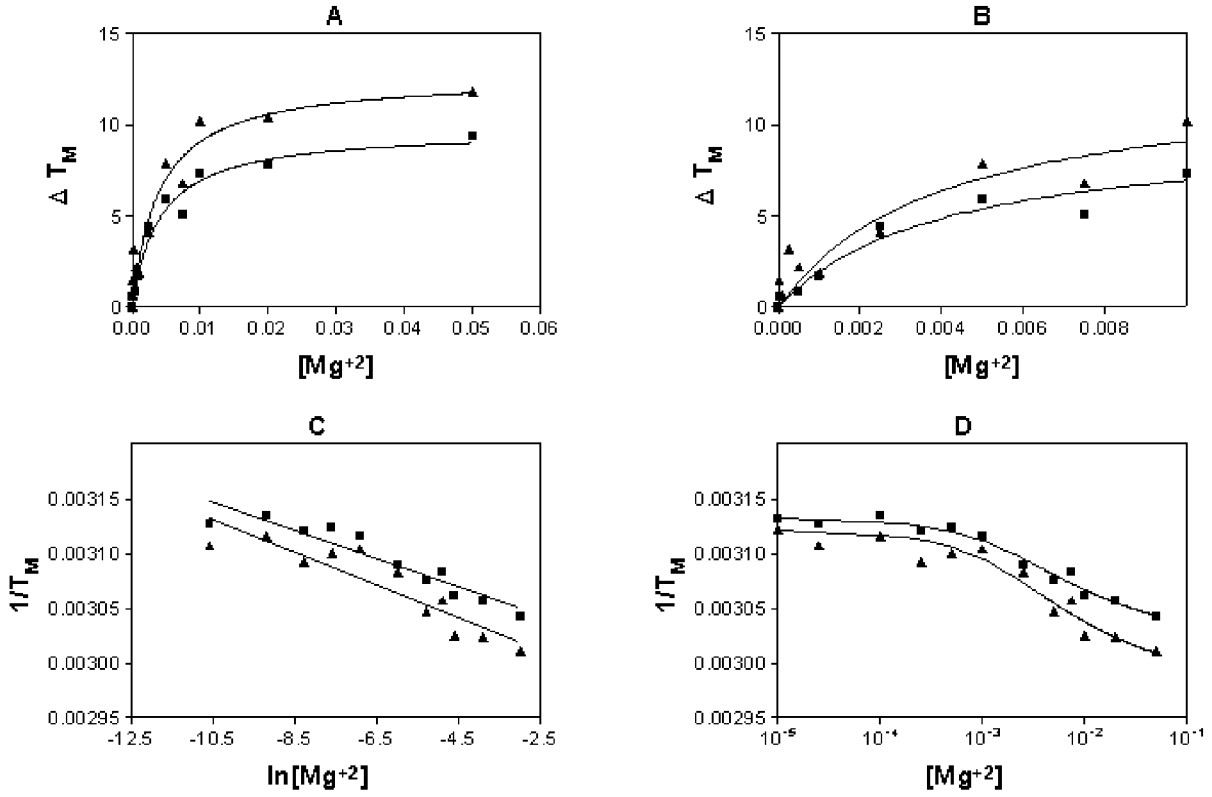

FIGURE 3. Stabilization of RNA oligomers with tandem GA base pairs by Mg^{2+}. **A,B**: Change in melting temperature (at 1×10^{-4} M oligomer) as a function of [Mg^{2+}], high (**A**) and low (**B**) magnesium concentrations. **C**: Reciprocal T_M plotted as a function of added Mg^{2+}. The lines are the least squares fit of the data to equation 1. **D:** Reciprocal T_M plotted as a function of added Mg^{2+}. The curves are the least squares fit of the data to equation 2. The T_M value at 10^{-5} M is the reciprocal melting temperature in the absence of Mg^{2+} and is not used in the fit. ▲: $(5'GGCGAGCC)_2$, ■: $(5'GGCAGGCC)_2$.

mation in 1 M NaCl melt buffer are within experimental error of those measured previously. The $\Delta G°_{37}$ value for the AG tandem pair is -0.2 kcal/mol.

The effect of Mg^{2+} ion on the thermal stability of the oligomers with tandem GA pairs is shown in Figure 3A,B. The melting temperature for the GA oligomer increases by 11.8 °C in 50 mM Mg^{2+} ion and that of the AG oligomer by 9.4 °C (Table 2). These increases are nearly the same as those observed for the regular Watson–Crick octamer duplex. The data for the tandem GA oligomers were then fitted to the two models for Mg^{2+} binding and the results are displayed in Figure 4C,D. Fitting the data to model 1 results in a slope that corresponds to Δn values of 0.52 (GA) and 0.40 (AG; Fig. 4C). The results suggest that neither of the tandem GA serve as a specific Mg ion-binding site; in fact, there is a smaller change in Δn relative to the same sized regular Watson–Crick duplex. The data again present a distinctive sigmoidal shape. The values for K_f are 430 M^{-1} and 260 M^{-1} and for K_u 130 M^{-1} and 84 M^{-1} for GA and AG, respectively, and are obtained from the fit to model 2 (Fig. 4D). The results are summarized in Table 3. Surprisingly, these results suggest that Mg^{2+} ions interact about the same or slightly less favorably with tandem pairs of non-Watson–Crick GA than with Watson–Crick base pairs, at least within regular helices.

The results of BD simulations are shown in Figures 5 and 6. Figure 5A displays the geometry of the tandem GA pair and Figure 5B shows the helix structure with the narrow deep groove produced by the *trans* Hoogsteen/sugar edge GA pairs. The BD simulation shows an accumulation of metal-binding sites within the deep groove. The narrow deep groove of the tandem GA helix features high occupancy sites for both 1.2- and 2.2-Å spheres near the center of the helix (Fig. 5B). Again, space-filling representations of the low occupancy sites (Fig. 5C) indicate that the deep groove is lined with potential binding sites. Figure 6A displays the geometry of the tandem AG pair and Figure 6B shows the helix structure with the widened deep groove produced by the *cis* Watson–Crick/Watson–Crick AG pairs. The BD simulation shows an accumulation of metal binding sites within the deep groove (Fig. 6B). The wider deep groove of the tandem AG helix features high occupancy sites not only at the center of the helix (near the AG pairs) but also near the helix ends for the 1.2-Å spheres. The high occupancy 2.2-Å spheres sites are located

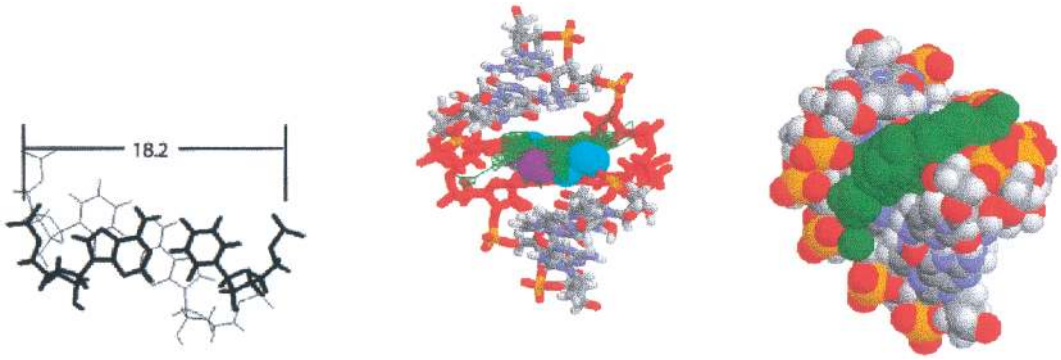

FIGURE 4. Left: Geometry of two Watson–Crick base pairs with A-form structure. The base pair in dark lines is closer to the reader that the lighter pair. Distance is phosphate–phosphate distance for the closest base pair in Ångstroms. Middle: Magnesium binding sites determined by BD simulation on crystal structure of A-form RNA hexamer. Volume elements of high occupancy for the +2 charged test spheres are visualized as cyan (1.2 Å) and purple (2.2 Å) spheres. Volume elements of low occupancy are visualized as green polyhedra. Right: Volume elements of low occupancy are visualized as green spheres.

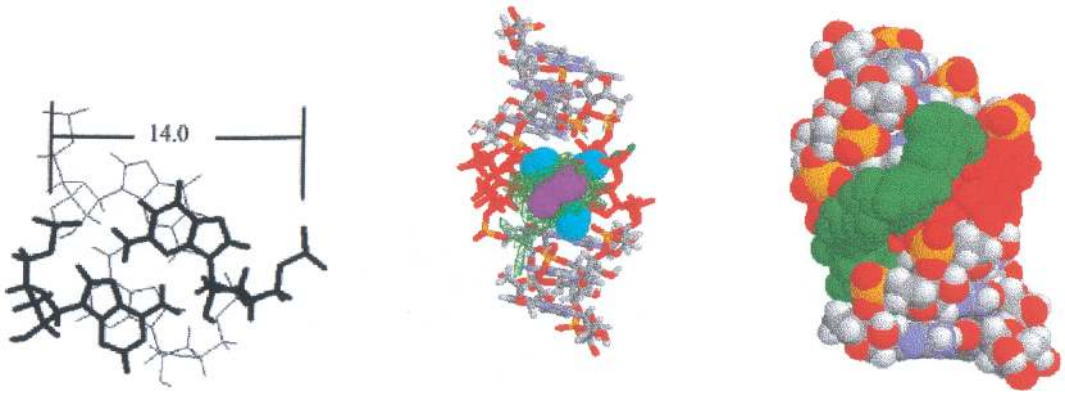

FIGURE 5. Left: Geometry of two "sheared" tandem AG base pairs. The base pair in dark lines is closer to the reader than the lighter pair. Distance is phosphate–phosphate distance for the closest base pair in Å. Middle: Magnesium binding sites determined by BD simulation on crystal structure of GGCGAGCC. Tandem GA pairs are shown in red. Volume elements of high occupancy for the +2 charged test spheres are visualized as cyan (1.2 Å) and purple (2.2 Å) spheres. Volume elements of low occupancy are visualized as green polyhedra. Right: Volume elements of low occupancy are visualized as green spheres.

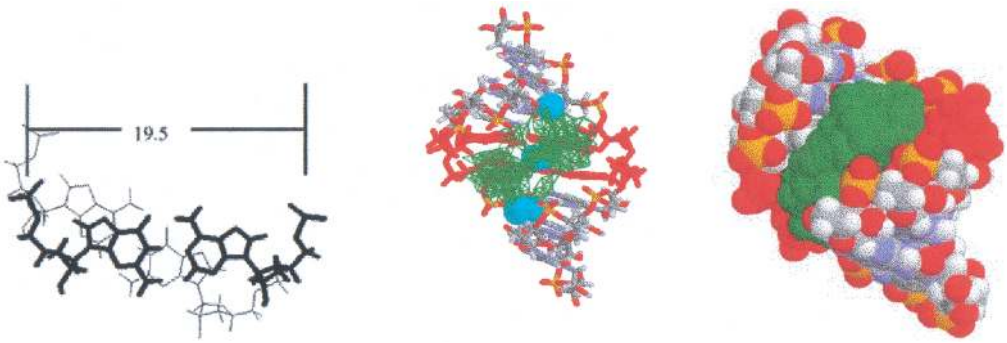

FIGURE 6. Left: Geometry of two tandem non-Watson–Crick GA base pairs. The base pair in dark lines is closer to the reader than the lighter pair. Distance is phosphate–phosphate distance for the closest base pair in Å. Middle: Magnesium binding sites determined by BD simulation on crystal structure of GGCAGGCC. Tandem AG pairs are shown in red. Volume elements of high occupancy for the +2 charged test spheres are visualized as cyan (1.2 Å) and purple (2.2 Å) spheres. Volume elements of low occupancy are visualized as green polyhedra. Right: Volume elements of low occupancy are visualized as green spheres.

at the center of the helix. The low occupancy sites modeled in Figure 6C as spheres line the deep groove.

Phylogenetic analysis of rRNAs has shown that the symmetrical sequence 5′-UG/GU is the most prevalent non-Watson–Crick tandem (Gutell et al., 1992; Gutell, 1994). This motif has been shown to be more stable than other tandem non-Watson–Crick pairs (He et al., 1991). The tandem GU in the opposite orientation 5′GU/UG is less prevalent (Gautheret et al., 1995) and its stability depends upon the identity of the flanking base pairs (Wu et al., 1995). The nonsymmetrical 5′GG/UU tandem motif is intermediate both in abundance and stability relative to the two symmetrical GU motifs (Gautheret et al., 1995; Xia et al., 1997). The structure and properties of GU pairs and tandem have recently been reviewed (Masquida & Westhof, 2000). The structures of three different tandem GU pairs have been determined by X-ray diffraction (Biswas & Sundaralingam 1997; Biswas et al., 1997; Trikha et al., 1999). In each case, oligomers with UG, GU, and GG tandem pairs provide potential metal-binding sites with unique structural features (Figs. 8, 9, 10). Tandem GU pairs have been shown to be metal-binding sites in the P4–P6 domain of the Group I intron (Cate & Doudna, 1996). Additionally, Kieft and Tinoco (1997) have shown the binding of cobalt (III) hexammine to tandem GU base pairs in solution. We investigated three oligomers containing tandem GU in different orientations, (5′GCA**UG**UGC)$_2$, (5′GCA**GU**UGC)$_2$, and 5′GCU**GG**UGC/3′CGA**UU**AGC (see Table 1).

The stability of the GU tandem base pairs have been previously measured in standard 1.0 M NaCl melt buffer (Mathew et al., 1999, and reference therein). The ΔG°_{37} of the (5′GCA**UG**UGC)$_2$ oligomer measured here is −8.4 kcal/mol (Table 1). The stability increment of the tandem UG base pair measured here is −2.1 kcal/mol at 37 °C, which is similar to the stability (−1.7 kcal/mol) of the UG base pair in the in the oligomer (5′GGA**UG**UC)$_2$ measured previously (He et al., 1991). The stability of the GU oligomer measured here (ΔG°_{37} = −6.0 (Table 1)) is much lower than for the UG oligomer, indicative of the lower stability of the GU tandem base pair. The stability of the tandem GU base pair increment determined from our data is +0.2 kcal/mol, a value close to the +0.5 kcal/mol measured for other tandem GU pairs (McDowell et al., 1997). The stability (ΔG°_{37}) of the GG oligomer (5′GCU**GG**UGC/3′CGA**UU**AGC) is −7.6 kcal/mol. The ΔG°_{37} contribution of the GG/UU tandem base pair is found to be −1.5 kcal/mol for the GG oligomer. As expected, the GG/UU tandem base pair is intermediate in stability between the UG and GU tandem base pairs (He et al., 1991).

Figure 7 displays the effect of Mg^{2+} ion concentration on the thermal stability of the three oligomers with tandem GU pairs. The addition of 50 mM Mg^{2+} ions to the 0.1 M NaCl melt buffer increases the melting temperature of the UG, GU, and GG/UU oligomers 10, 12, and 10 °C, respectively (Table 2). The changes in melting temperatures with added Mg^{2+} ions are again less than or equal to those observed for the octamer Watson–Crick duplexes. The data were fitted to model 1 (Fig. 7C). From the slope of the $1/T_M$ versus ln[Mg^{2+}] plot, the Δn values for the three oligomers are again less than those for the Watson–Crick duplexes (Table 3). The data present a distinctive sigmoidal shape and the fits to model 2 are shown in Figure 7D with the derived binding constants listed in Table 3. The magnesium ion binding constants to the helical forms of the GU oligomers vary between 91 and 310, indicating a weaker interaction with these oligomers than to the octamer with only Watson–Crick base pairs. The magnesium ion binding constants to the single-stranded forms of the GU oligomers are also less than or equal to the binding constant to the single-stranded octamer sequence with only Watson–Crick base pairs. Additionally, the ratios of K_f/K_u for the GU oligomers are smaller than that observed for the Watson–Crick octamer. The difference in binding constants between the helical and single-stranded GU containing RNA oligomers are less than what was observed for the fully Watson–Crick base-paired RNAs. However, among the "GU" tandem oligomers, the values of K_f and K_u for the GG/UU tandem are rather different from those of the other two GU tandems. In addition, the $\Delta\Delta H$ value for the GG/UU tandem oligomer (12 kcal/mol) in 50 mM magnesium ion buffer relative to the 0.1 M NaCl melt buffer is 50% higher than those for the other "GU" tandem oligomers (8 kcal/mol; Table 1). Interestingly, in the crystal structure of the P4–P6 fragment (Cate & Doudna, 1996), the GG/UU tandem is the only one observed to bind both cobalt hexammine and magnesium ions. The GG/UU motif has also been found to bind cobalt hexammine ions in solution (Kieft & Tinoco, 1997).

The results of BD simulations for the oligomer ((5′GUA**UG**UA)dC)$_2$ containing the tandem UG base pair (Biswas et al., 1997) are shown in Figure 8B. The high occupancy sites are located at the center of the helix adjacent to the UG pairs (Fig. 8B), and lower occupancy sites line again the deep groove (Fig. 8C). BD simulations with the oligomer sequence containing a tandem GU motif (Biswas & Sundaralingam, 1997) generated the results seen in Figure 9B. The high occupancy sites are localized near the center of the deep groove adjacent to the GU pairs (Fig. 9B) and lower occupancy sites line the entire deep groove (Fig. 9C). The geometry of the tandem nonsymmetrical GG/UU wobble base pairs were determined in crystals of an RNA duplex with the sequence (5′GGUAUUGC GGUACC)$_2$ (Trikha et al., 1999; Fig. 10A). The longer sequence used in this BD simulation leads to a greater accumulation of high occupancy sites in the deep groove near the center of the sequence (Fig. 10B). However, rather than being directed near the tandem GG/UU

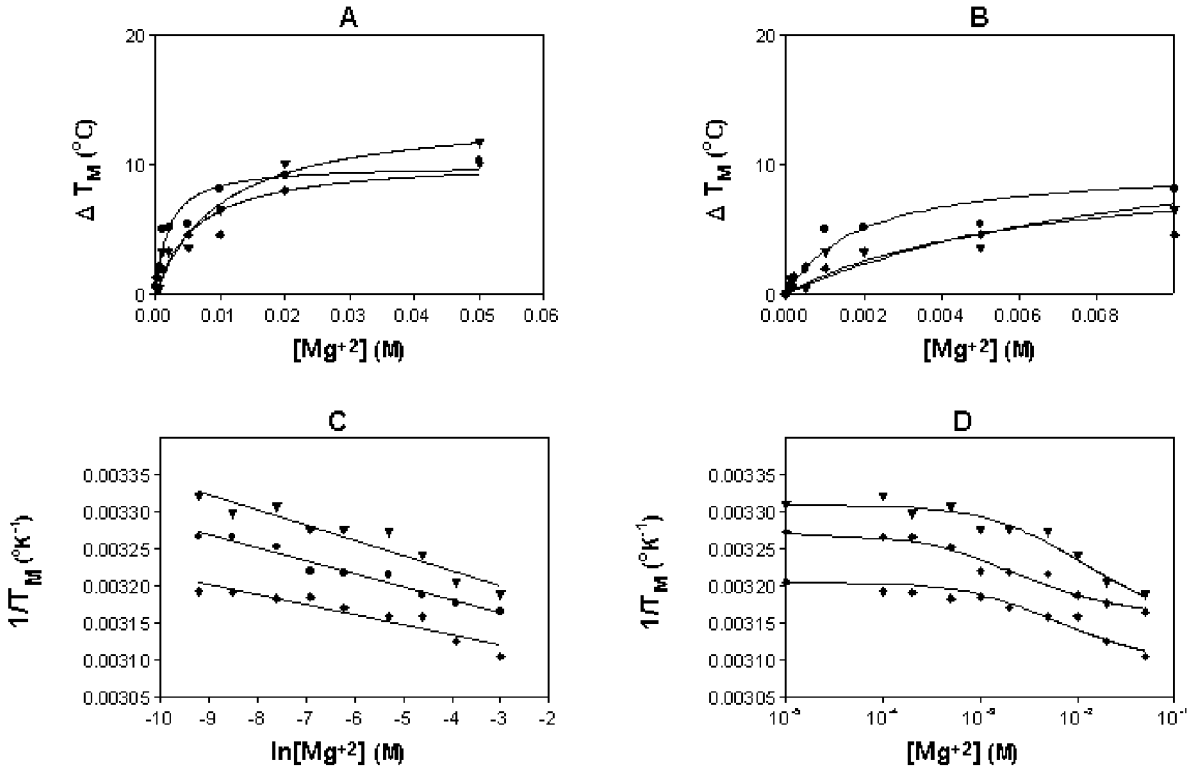

FIGURE 7. Stabilization of RNA oligomers with tandem GU base pairs by Mg^{2+}. **A**,**B**: Change in melting temperature (at 1×10^{-4} M oligomer) as a function of [Mg^{2+}], high (**A**) and low (**B**) magnesium concentrations. **C**: Reciprocal T_M plotted as a function of added Mg^{2+}. The lines are the least squares fit of the data to equation 1. **D**: Reciprocal T_M plotted as a function of added Mg^{2+}. The curves are the least squares fit of the data to equation 2. The T_M value at 10^{-5} M is the reciprocal melting temperature in the absence of Mg^{2+} and is not used in the fit. ♦: $(5'GCAUGUGC)_2$, ▲: $(5'GCAGUUGC)_2$, ●: (5′GCUGGUGC/3′CGAUUACG).

pairs, the highest occupancy sites are located near the GC base pairs located between the tandem wobble pairs. Low occupancy sites line the entire deep groove of the oligomer (Fig. 10C).

Motifs larger than tandem non-Watson–Crick pairs were then investigated. The eubacterial loop E of *Escherichia coli* 5S RNA comprises a large number of noncanonical base pairs within a 7×7 symmetrical internal loop. It requires millimolar Mg^{2+} to adopt its ordered structure (Leontis et al., 1986; Romby et al., 1988). The crystal structure (Correll et al., 1997) contains a number of bound metal ions and BD simulations yielded metal-binding sites corresponding to several ion positions seen in the crystal (Hermann & Westhof, 1998). The two variants of the eubacterial loop E motif studied here $(5'GCC\mathbf{GAUGGUA}GCC)_2$, a loop E duplex, and the same loop E motif within a hairpin loop, contains the consensus eubacterial loop E sequence flanked by Watson–Crick pairs. The eukaryotic loop E motif is an asymmetric 4×3 internal loop, identical with the loop sequence and structure of the sarcin-ricin loop of 23S rRNA that has been solved by NMR (Wimberly et al., 1993; Szewczak & Moore, 1995) and X-ray diffraction (Correll et al., 1999). The eukaryotic loop E internal loop is characterized by a bulged G residue with the AGUA motif flanked by Watson–Crick pairs. BD simulations have suggested three potential, but delocalized, metal-binding sites in the sarcin-ricin loop (Hermann & Westhof, 1998) and, interestingly, the crystal structure of the sarcin-ricin loop has neither monovalent nor divalent metal ions bound to the RNA (Correll et al., 1999).

The influence of Mg^{2+} ion on the stability of RNA oligomers containing the loop E motifs is shown in Figure 11. The melting data could not be collected over the full range of Mg^{2+} ion concentrations for either the loop E hairpin or eubacterial loop E duplex. The loop E hairpin oligomer precipitates above 2 mM Mg^{2+}. The T_M value for the loop E hairpin increased by 11 °C in the 2 mM Mg^{2+} buffer, nearly as large a change as was observed for the duplexes and tandem GA and GU oligomers in 50 mM Mg^{2+} (Fig. 11). In fact, none of the other oligomers have an increase in melting temperature of more than 5 °C in 2 mM Mg^{2+} melt buffer. The melting curves of the eubacterial loop E as a duplex present a second transition above 20 mM Mg^{2+} concentration and the melts decreased in hyperchromicity upon repeated melting and therefore could not be analyzed. The results display two remarkable features.

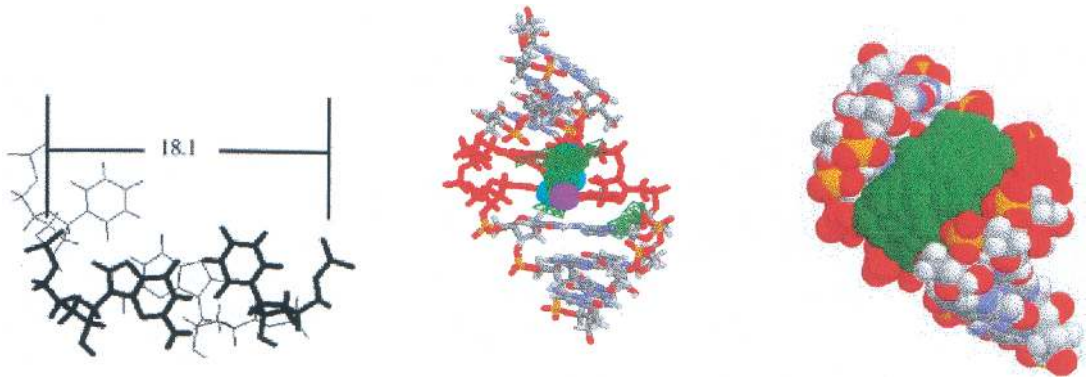

FIGURE 8. Left: Geometry of two tandem UG pairs. The base pair in dark lines is closer to the reader than the lighter pair. Distance is phosphate–phosphate distance for the closest base pair in Å. Middle: Magnesium binding sites determined by BD simulation on crystal structure of (GUAUGUA)dC_2. Tandem UG pairs are shown in red. Volume elements of high occupancy for the +2 charged test spheres are visualized as cyan (1.2 Å) and purple (2.2 Å) spheres. Volume elements of low occupancy are visualized as green polyhedra. Right: Volume elements of low occupancy are visualized as green spheres.

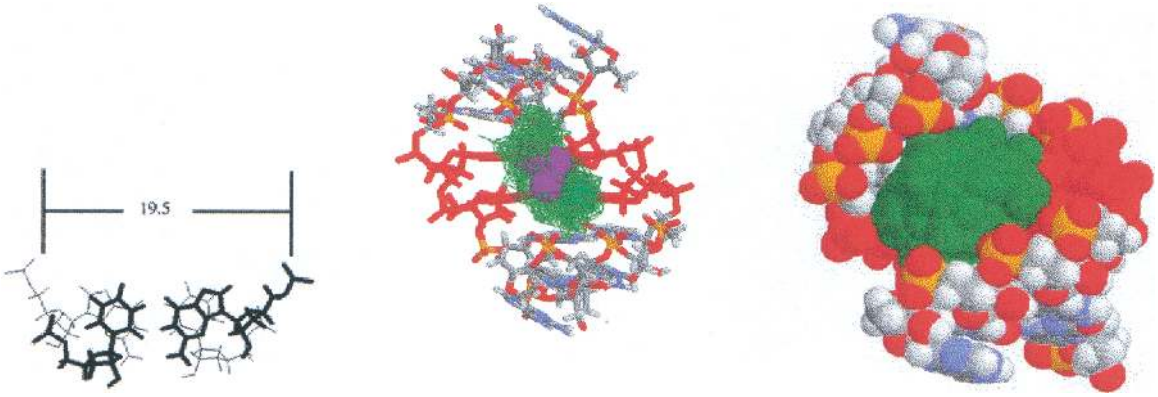

FIGURE 9. Left: Geometry of two tandem GU pairs. The base pair in dark lines is closer to the reader thaN the lighter pair. Distance is phosphate–phosphate distance for the closer base pair in Ångstroms. Middle: Magnesium binding sites determined by BD simulation on crystal structure of (GUGUGUA)dC_2. Tandem GU pairs are shown in red. Volume elements of high occupancy for the +2 charged test spheres are visualized as cyan (1.2 Å) and purple (2.2 Å) spheres. Volume elements of low occupancy are visualized as green polyhedra. Right: Volume elements of low occupancy are visualized as green spheres.

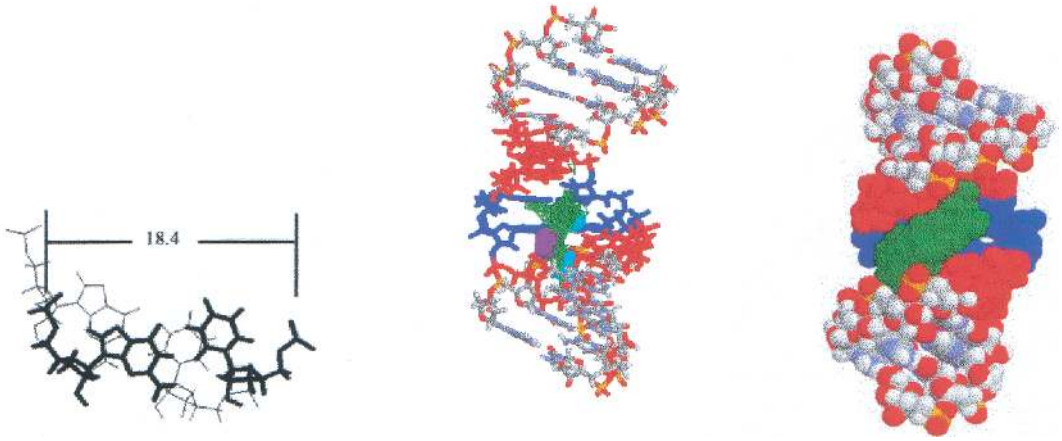

FIGURE 10. Left: Geometry of two tandem GG/UU pairs. The base pair in dark lines is closer to the reader than the lighter pair. Distance is phosphate–phosphate distance for the closest base pair in Å. Middle: Magnesium binding sites determined by BD simulation on crystal structure of GGUAUUGCGGUACC$_2$. Tandem GG/UU pairs are shown in red and noncanonical Watson–Crick GC base pairs are shown in blue. Volume elements of high occupancy for the +2 charged test spheres are visualized as cyan (1.2 Å) and purple (2.2 Å) spheres. Volume elements of low occupancy are visualized as green polyhedra. Right: Volume elements of low occupancy are visualized as green spheres.

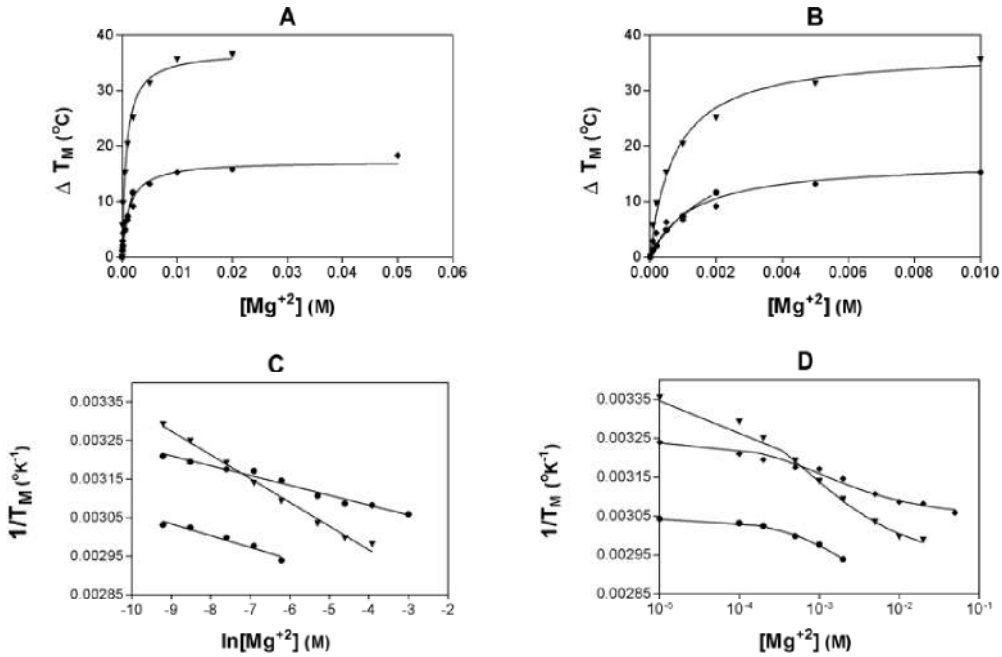

FIGURE 11. Stabilization of RNA oligomers with loop E motifs by Mg^{2+}. **A,B:** Change in melting temperature (at 1×10^{-4} M oligomer) as a function of [Mg^{2+}], high (**A**) and low (**B**) magnesium concentrations. **C**: Reciprocal T_M plotted as a function of added Mg^{2+}. The lines are the least squares fit of the data to equation 1. **D**: Reciprocal T_M plotted as a function of added Mg^{2+}. The curves are the least squares fit of the data to equation 2. The T_M value at 10^{-5} M is the reciprocal melting temperature in the absence of Mg^{2+} and is not used in the fit. ♦: eukaryotic loop E, ●: loop E hairpin, ▼: eubacterial loop E.

First, the extent of stabilization of the eubacterial loop E duplex far exceeds the stabilizations seen previously. The value of the melting temperature increases by more than 36 °C in 20 mM Mg^{2+} ion (Fig. 11A,B). Second, there is a sharpening of the melting transition indicative of an increase in the van't Hoff enthalpy for the transition. The increase in van't Hoff enthalpy for a transition may arise either from a change in the heat released during the transition or an increase in the cooperativity of the transition. Typical melting curves are displayed in Figure 12. In the absence of Mg^{2+} ion, the eubacterial loop E duplex displays very little hyperchromicity (5–7%). Mg^{2+} ion increases the hyperchromicity (10–20%) for the melts and sharpens the melting transition. Figure 13 displays the change in van't Hoff enthalpy for the melting transition of the eubacterial loop E duplex as a function of Mg^{2+} ions. For comparison, the van't Hoff enthalpies for melting of a duplex $(5'CCAUAUGG)_2$, the eukaryotic loop E (AGUA), and the eubacterial loop E hairpin are also plotted. Only the eubacterial loop E motifs display a significant trend in the van't Hoff enthalpy of the transition with increasing Mg^{2+} ion concentration. The duplex $(5'CCAUAUGG)_2$ and the eukaryotic loop E motif have slight increases in enthalpy with increasing Mg^{2+} in concentration. The van't Hoff enthalpy changes observed for these oligomers suggest that, as observed previously (Leontis et al., 1986; Romby et al., 1988), correct folding of the eubacterial loop E motif requires Mg^{2+} ion. These results further point to a distinctly different mode of interaction of the eubacterial loop E RNA with Mg^{2+} ion relative to the other oligomers studied (see below).

An increase in the van't Hoff enthalpy change upon disruption of tertiary structure by Mg^{2+} ion for a 59-nt fragment of rRNA (Laing et al., 1994) and the *td* intron of bacteriophage T4 (Brion et al., 1999) has previously been observed. The addition of 20 mM Mg^{2+} ion increased the change in van't Hoff enthalpy by about

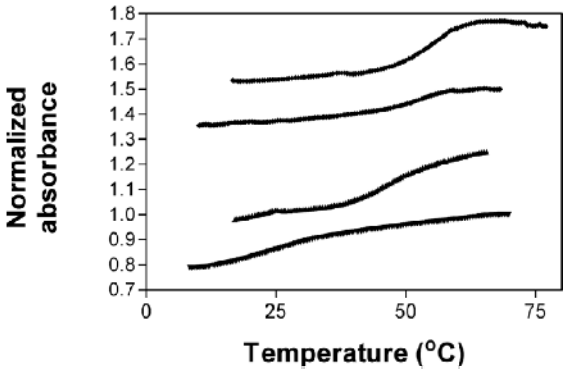

FIGURE 12. Normalized melting curves for the eubacterial loop E duplex. The curves are offset by 0.25 for clarity. Curves from bottom to top are for 0.1 M NaCl melt buffer containing 0.0, 0.2, 2.0, and 20 mM $MgCl_2$.

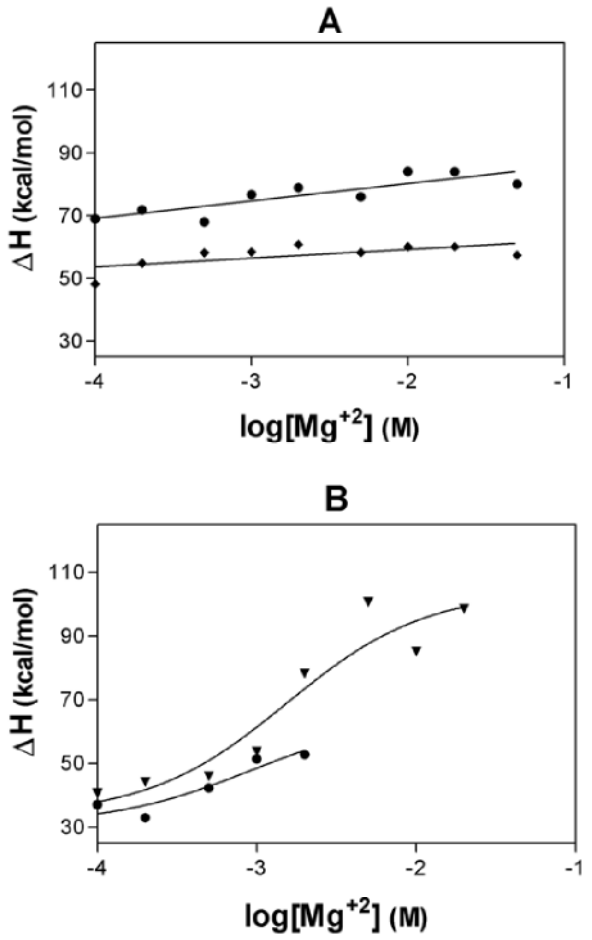

FIGURE 13. Magnesium ion effect on the enthalpy of duplex formation. **A**: ●: $(5'CCAUAUGG)_2$, ♦: eukaryotic loop E. **B**: ●: loop E hairpin, ▼: eubacterial loop E.

15 kcal/mol for the 59-nt fragment of rRNA and 260 kcal/mol for the *td* intron (269-nt construct). The increase in van't Hoff enthalpy during melting in the presence of Mg^{2+} ions observed here for the eubacterial loop E tertiary structure is nearly 60 kcal/mol (also 20 mM) and more than twofold higher than in the absence of Mg^{2+} ions. The melting temperature for the eubacterial loop E duplex also increases significantly in the 1.0 M NaCl buffer relative to the 0.1 M NaCl buffer (Table 1). The increase of over 20 °C in the melting temperature is over two times greater than that observed for any of the other oligomers. In addition, there is also a significant increase in the enthalpy of melting 66 versus 42 kcal/mol, respectively. It appears that high monovalent ions (1.0 M) are able to stabilize the loop E structure but not to the same extent as 20 mM Mg^{2+} ion (Table 2). The melting temperature for the eukaryotic loop E oligomer increases by 11.4 °C upon the addition of 50 mM Mg^{2+} ion (Table 2), an increase similar to that observed for the other oligomers.

There are too few data points for any further analysis of the loop E hairpin. The effect of Mg^{2+} ion is much greater on the stability of the eubacterial duplex loop E than on any of the other duplexes investigated. The change in melting temperature for the 20 mM Mg^{2+} ion buffer is more than 1.6 times as large as that for the 1.0 M NaCl buffer (Table 2). The observed ratio is small due of the unusually large T_M change observed upon the addition of 1.0 M NaCl. The effect is more striking in terms of ΔG°_{37} where the value increases to 13.7 kcal/mol in 20 mM Mg^{2+} ion melt buffer compared to 4.8 kcal/mol in the absence of magnesium ion. This increase is three times larger than that observed for any of the other oligomers (Table 2). The relative effect of Mg^{2+} ion on the eukaryotic loop E motif is similar to that observed with the other oligomers investigated. The ratio of the changes in melting temperature in 50 mM magnesium ion relative to the change to 1.0 M NaCl is 1.9 and the relative change in ΔG°_{37} is 2.0 (Table 2).

The data were fitted to model 1 for the binding of Mg^{2+} ion to the oligomers (Fig. 11C). The large change in the values for the melting temperature and enthalpy for the eubacterial loop E duplex complicates the analysis of the magnesium binding data, as the melting transition seems to be changing with Mg^{2+} ion concentration. Fitting the eubacterial loop E duplex data to model 1 and using an average enthalpy for the transition of −65.5 kcal/mol produces, as expected, a larger Δn than seen for the other oligomers: 2.1 (Table 3). As opposed to the other oligomers, the data are linear over a 100-fold Mg^{2+} ion concentration range (0.1–10 mM). The eukaryotic loop E data is also linear over the entire range of magnesium ion concentrations investigated, albeit with a much smaller slope. The Δn determined from the fit for the eukaryotic loop E oligomer data is 0.7 (Table 3). The results show that for the latter oligomer, less than one additional Mg^{2+} ion binds upon duplex formation.

The results of fitting the data to model 2 are shown in Figure 11D and the derived binding constants are presented in Table 3. The binding constant for Mg^{2+} ion derived from the data for the single-stranded eubacterial loop E duplex, 250 M^{-1}, is similar to the binding constant for the 14mer oligomer (Table 3). As expected from the data, the fitting produces a binding constant to the helical form that is 10 times larger than the binding constant to the single-stranded form. These results suggest that the interaction of Mg^{2+} ion with the eubacterial loop E duplex is fundamentally different from that observed for the other oligomers. It would not be unreasonable to suspect that one or a few Mg^{2+} ions are in fact interacting in a specific manner with the eubacterial loop E motif. The eubacterial loop E data were, therefore, fitted to a combination of models 1 and 2 to take into consideration both specific and nonspecific binding (Laing et al., 1994). The nonspecific binding was fixed with $m = 24$, the number of phosphates, with K_f and K_u, of 840 M^{-1} and 310 M^{-1}, respectively, the values expected for a 13mer (Fig. 2). The Δn derived

from this fit was 1.2 irrespective of the starting value, and the binding constant for the Mg^{2+} ion was 40,000 M^{-1} (Table 3). This binding constant is similar to the specific Mg^{2+} ion binding to tRNA measured by equilibrium dialysis (Stein & Crothers, 1976). On the other hand, the increase in the affinity of Mg^{2+} ion upon duplex formation for the eukaryotic loop E motif is less than fourfold, in fact, less than that observed for the other duplexes studied and are again indicative of a rather modest interaction with Mg^{2+} ions.

DISCUSSION

Increasing the NaCl concentration from 0.1 M to 1.0 M increased the melting temperature and thermal stability of all of the oligomers investigated. The extent of change is related to the size of the oligomer (Table 2). The hexanucleotide oligomer has about an 8 °C higher melting temperature, the octanucleotide oligomers about an 8–10 °C higher melting temperature, and the 14mer has about a 13 °C higher melting temperature in 1.0 M NaCl than 0.1 M NaCl. It is more difficult to compare the loop E motifs. The eukaryotic loop E motif AGUA/AUG has about the expected melting temperature change, 9 °C. The loop E hairpin change in T_M is less than expected based upon the length of the stem, but this may be related to the hairpin loop structure or conversely, counterion condensation may be more important for the longer (28 nt) length of the hairpin single-stranded structure. The eubacterial loop E as a duplex displays not only an unusually large change in melting temperature, but also a large $\Delta\Delta H^\circ$. It appears that 1.0 M Na^+ ion is able to partially stabilize the eubacterial loop E motif (Table 1). The tandem GU duplex had a similar change in $\Delta\Delta H^\circ$ with changes from 0.1 to 1.0 M Na^+ ion, without a concomitant large change in T_M.

The addition of 50 mM Mg^{2+} ion to the 0.1 M melt buffer produces greater changes in T_M than those observed in the 1.0 M melt buffer for all of the oligomers investigated except for the 14mer duplex, where the increase in melting temperature was 2 °C less, and the UG oligomer, which has approximately the same ΔT_M (Table 2). This is true despite the overall lower ionic strength of the 50 mM Mg^{2+} buffer. Except for the eubacterial loop E oligomers, the effect of magnesium ions on the stability of the RNAs is relatively modest. For the duplexes and tandem GA and GU oligomers, the addition of 50 mM Mg^{2+} ions to the melt buffer increases the melting temperature by 9–12 °C and the free energy by 2–3 kcal/mol. The eukaryotic loop E oligomer has a much larger increase in T_M (16.3 °C) but only a modest increase in free energy (3 kcal/mol). Although we were only able to study the eubacterial loop E duplex in Mg^{2+} ion buffers up to 20 mM, the effects are dramatic with an increase in melting temperature of nearly 37 °C, a $\Delta\Delta G^\circ_{37}$ of 8.9 kcal/mol, and an increase in $\Delta\Delta H^\circ$ of 57 kcal/mol.

The results for the fitting of the change in melting temperature versus the Mg^{2+} ion concentration are summarized in Table 3. When the data are fitted to model 1, the results can be interpreted as due to a change in the number of Mg^{2+} ions binding to the oligomer upon secondary structure formation. The Δn values for the Watson–Crick duplexes are related to size with the longer oligomers having the larger Δn. However, on a per phosphate basis, the smaller oligomers displayed the larger change. In no case, except the eubacterial loop E duplex, were the Δn values greater than 1. The Δn values determined from the slope of the Δ_M versus $\ln[Mg^{2+}]$ lines for the duplexes were in fact larger on a per phosphate basis than for any of the oligomers with secondary structure motifs investigated, except the eubacterial loop E duplex. These results seem to indicate that, despite the presence of numerous ligands in the altered deep groove formed by the tandem non-Watson–Crick base pairs, Mg^{2+} ions do not interact in any specific manner with the secondary structural motifs investigated, except the eubacterial loop E duplex. The change in stability of the oligomers due to Mg^{2+} ion can therefore be interpreted as a slight increase in affinity of a large number (number of phosphates/2) of ions upon folding the structures as in model 2 (Table 3). The binding constants for Mg^{2+} ion to the helical and single-stranded Watson–Crick oligomers increase with the length of the oligomer.

Magnesium ions appear to interact with the eubacterial loop E duplex oligomer in a distinctly different manner than with the other oligomers investigated. Fitting the data to model 2 for nonspecific metal ion binding produces values for the binding constants to the folded (2590 M^{-1}) form (Table 3) that is very different from the values observed for the other oligomers. The effect of Mg^{2+} ions on the enthalpy change for secondary structure formation also argues for a more complex mode of interaction. The data fitted to a model with both specific and nonspecific binding sites produces a reasonable interpretation of the results. Part of the Mg^{2+} ion stabilization is due to the nonspecific interaction of ions with the oligomer as observed for the other oligomers. This was modeled using the number of phosphates and the expected magnesium ion binding constants for a 13mer oligomer of folded (840 M^{-1}) and unfolded (310 M^{-1}) RNA obtained from Figure 2. The remainder of the Mg^{2+} ion stabilization can then be modeled as a specific interaction of the metal ion with the RNA. The fit leads to a single (1.2) high-affinity specific binding site with a binding constant of 40,000 M^{-1} (Table 3).

Is it possible to reconcile these results with crystal structures of RNAs in which several of these structural motifs clearly present bound Mg^{2+} ions? First, RNAs

are often crystallized from solutions of much higher Mg^{2+} ion concentrations, up to 500 mM (Masquida & Westhof, 1999) than those used in these studies. The ions seen in the crystals may therefore represent binding to very low-affinity sites. Second, Mg^{2+} ions observed in crystal structures (e.g., around the tandem GU base pairs) may, in addition, become kinetically trapped by the crystalline environment. A further complication arises from the fact that the occupancies of the ions bound to the various sites are difficult to refine properly and in several occurrences partial rather than full occupancy might be present. Indeed, some of the ions observed by crystallography could be seen not as statically bound but as exchanging with solvent molecules and other types of ions (e.g., monovalent ions). Thus, as with water molecules where one speaks of hydration sites, one might consider the structures derived from X-ray studies as revealing the potential sites for metal-ion binding.

Therefore, it appears that Mg^{2+} ion interactions with small RNA oligomers, even if they include tandem non-Watson–Crick pairs, can be explained by the binding of a cloud of delocalized ions that interacts more strongly with the duplex than the random coil structure. This view is supported by the Brownian dynamics simulations that display rather delocalized ionic densities, except for the eubacterial loop E, where precisely located densities were calculated (Hermann & Westhof, 1998). Indeed, with the eubacterial loop E, peculiar effects were observed in presence of Mg^{2+} ions: (1) a large increase in hyperchromicity with sharpening of the absorbance peak; (2) a concomitant large increase in the van't Hoff enthalpy change; and (3) a threefold increase in thermal stability (ΔG°_{37} 13.7 vs. 4.8 kcal/mol) relative to the addition of 1 M monovalent ion. The increase in van't Hoff enthalpy for a transition may arise from a change in the heat released during the transition, an increase in the cooperativity of the transition, or a combination of both. The energy of dehydration of Mg^{2+} ions is very large (about 455 kcal/mol). The large enthalpy changes observed upon folding could then imply that the cost of dehydrating some ions is more than compensated by the chelation of those ions to the RNA-binding pockets. At the same time, the binding of magnesium ions at specific locations could organize the internal loop in such a way that the two stems are coupled and melt cooperatively leading to a sharpening of the melting transition and an increase in the van't Hoff enthalpy. In any case, these observations point to specific chelations of Mg^{2+} ions by the folded structure of the eubacterial loop E sequence, as was suggested for the large group I introns where very similar effects have been analyzed (Brion et al., 1999). The crystal structure of the eubacterial loop E indeed shows the presence of four Mg^{2+} ions, three of which have lost one water molecule from their hydration shells. Presently, without measurement of the heat released, it is not possible to partition the component of those large enthalpy changes observed in the unfolding of RNA systems of varying complexity between variations in the hydration states and types of coordinating atoms in some specifically bound Mg^{2+} ions and changes in the cooperativity of the transition.

Are those measurements relevant to our understanding of RNA folding? It has recently been shown that RNA folding induced by Mg^{2+} ions leads, by counterion condensation, to a rapid collapse of the RNA towards compact (and, thus, with most of the secondary structure elements present) but still not fully native structures (Buchmueller et al., 2000; Heilman-Miller et al., 2000; Russell et al., 2000; Woodson, 2000). Native states with full tertiary interactions are observed afterwards at higher Mg^{2+} concentrations. Within this framework, the nonspecific, mainly through outer-sphere, binding of a cloud of delocalized ions interacting more strongly with the duplex than the random coil structure would then participate to the electrostatic collapse of the RNA. The specific chelation of some metal ions to partially preorganized RNA pockets, with the attached observed changes in hyperchromicity and enthalpy, would subsequently and with cooperativity lead to fully native structures.

MATERIALS AND METHODS

RNA synthesis and purification

Most oligomers were synthesized on solid support using the phosphoramidite approach. After ammonia and fluoride deprotection, the crude oligomer was purified by preparative TLC (*n*-propanol:ammonium hydroxide:water, 55:35:10) and Sep-Pak C18 (Waters) chromatography. Purities were checked by analytical TLC or electrophoresis and were greater than 95%. Some oligomers were synthesized by Dharmacon, deprotected using their procedures, and purified by gel electrophoresis.

Melting curves and data analysis

The buffer for the melting studies was 0.1 M NaCl, 10 mM cacodylic acid, pH 7, with varying concentrations of magnesium ion. Single-stranded extinction coefficients were calculated from the extinction coefficients for dinucleotide monophosphate and nucleosides (Borer, 1975; Richards, 1975). Strand concentrations were determined from high-temperature absorbance at 280 nm. Absorbance versus temperature curves were measured at 280 nm with a heating or cooling rate of 1.0 °C min^{-1}, on a Uvikon or a Beckman DU 640 spectrophotometer as described previously (Serra et al., 1994). Each data point represents the average of 10–20 melts of the oligomer. The oligomer concentrations were varied over at least a 50-fold range between 1 mM and 10 μM. Thermodynamics parameters for the oligomers were determined from both the average of the individual melt curves and plots of the reciprocal melting temperature (T_M^{-1}) versus the logarithm of the strand concentration (log $C_t/4$) for non-self-complementary se-

quences. Tables with the thermodynamics for each oligomer at the various magnesium ion concentrations investigated are available at http://webpub.alleg.edu/employee/m/mserra/professional/publications.shtml and http://www-ibmc.u-strasbg.fr/upr9002/westhof/.

Absorbance versus temperature profiles were fit to a two-state model with sloping base lines by using a nonlinear least squares program (McDowell & Turner, 1996). Thermodynamic parameters for duplex formation were obtained from the averages of the fits of the individual melting curves and by plotting the reciprocal of the melting temperature T_M^{-1} versus $\ln(C_t)$ for self-complementary or $\ln(C_t/4)$ for non-self-complementary sequences.

Initially, the sequences 5′-GCU**GAG**UGC/CGA**AUG**ACG-5′ and 5′-GCU**GAU**UGC/CGA**AUG**ACG-5′ were investigated. In the loop E motif, the GAG/AUG and GAU/AUG submotifs form similar single cross-strand purine stacks (Leontis & Westhof, 1998; Moore, 1999). Unfortunately, neither of these oligomers melted in a two-state manner. The first had a melting transition below 20 °C and the second displayed no hyperchromicity.

Brownian dynamics

Atomic coordinates were extracted from the Brookhaven Protein Data Bank (PDB) for duplex A-form RNA, 377D; AG tandem, 1MWG; GA tandem, 1YFV; GU tandem, 332D; UG tandem, 315D; GG tandem, 433D. For the NMR-derived structures, the first coordinate set was chosen. For the crystal structures, the metal ions and solvent were removed and hydrogen atoms added using the biopolymer module of Insight II. BD simulations were performed as previously described (Hermann & Westhof, 1998). From the trajectories that stayed inside the cutoff sphere, the final 100 recorded steps were used in the evaluation. The probabilities were visualized as a density grid superimposed on the RNA structure. High occupancy sites were defined as containing greater than 50 trajectories within the volume element.

ACKNOWLEDGMENTS

MJS was supported by a Fogarty Senior International Fellowship FO6 TW02345–01. We wish to thank Sarah Woodson and the anonymous referees for their useful comments. This work was supported by National Science Foundation Grants 9707940 and 0075962 (MJS). We thank the Fondation pour la Recherche Médicale for a grant (FRM 20000106/6-E) for the purchase of a UV spectrophotometer Uvikon 943 (Bio-Tek Instruments).

Received August 23, 2001; returned for revision September 18, 2001; revised manuscript received December 3, 2001

REFERENCES

Anderson CF, Record MT. 1995. Salt–nucleic acid interactions. *Annu Rev Phys Chem 46*:577–700.

Banerjee AR, Jaeger JA, Turner DH. 1993. Thermal melting of a group I ribozyme: The low temperature transition is primarily disruption of tertiary structure. *Biochemistry 32*:153–163.

Batey RT, Rambo RP, Doudna JA. 1999. Tertiary motifs in RNA structure and folding. *Anew Chem Int Ed 38*:2326–2343.

Biswas R, Sundaralingam M. 1997. Crystal structure of r(GUGUGUA)dC with tandem G × U/U × G wobble pairs with strand slippage. *J Mol Biol 270*:511–519.

Biswas R, Sundaralingam M. 1998. 1.76 Å structure of a pyrimidine start alternating A-RNA hexamer r(CGUAC)dG. *Acta Crystallogr D Biol Crystallogr 54*:570–576.

Biswas R, Wahl MC, Ban C, Sundaralingam M. 1997. Crystal structure of an alternating octamer r(GUAUGUA)dC with adjacent GU wobble pairs. *J Mol Biol 267*:1149–1156.

Borer PN. 1975. In: Fasman GD, ed. *Handbook of biochemistry and molecular biology: Nucleic acids*, 3rd ed. Cleveland, OH: CRC Press. p 589.

Brion P, Michel F, Schroeder R, Westhof E. 1999. Analysis of the cooperative thermal unfolding of the td intron of bacteriophage T4. *Nucleic Acids Res 15*:2494–2502.

Brion P, Westhof E. 1997. Hierarchy and dynamics of RNA folding. *Annu Rev Biophys Biomol Struct 26*:113–137.

Buchmueller KI, Webb AE, Richardson DA, Weeks KM. 2000. A collapsed non-native RNA folding state. *Nat Struct Biol 7*:362–366.

Cate JH, Doudna JA. 1996. Metal-binding site in the major groove of a large ribozyme domain. *Structure 4*:1221–1229.

Cole PE, Yang SK, Crothers DM. 1972. Conformational changes of transfer ribonucleic acid. Equilibrium phase diagrams. *Biochemistry 23*:4258–4368.

Correll CC, Freborn B, Moore PB, Steitz TA. 1997. Metals, motifs, and recognition in the crystal structure of a 5S rRNA domain. *Cell 91*:705–712.

Correll CC, Wool IG, Munishkin A. 1999. The two faces of the *Escherichia coli* 23 S rRNA sarcin/ricin domain: The structure at 1.11Å resolution. *J Mol Biol 292*:275–287.

Fieg AL, Uhlenbeck OC. 1999. The role of metal ions in RNA biochemistry. In: Gesteland RF, Cech TR, Atkins JF, eds. *The RNA World*. Cold Spring Harbor, New York: Cold Spring Harbor Press. pp 287–320.

Freier SM, Sinclair A, Neilson T, Turner DH. 1985. Improved free energies for GC base-pairs. *J Mol Biol 185*:645–647.

Gautheret D, Konings D, Gutell RR. 1995. GU base pairing motifs in ribosomal RNA. *RNA 1*:807–814.

Gutell RR. 1994. Collection of small subunits (16S- and 16S-like) ribosomal RNA structures. *Nucleic Acids Res 22*:3502–3507.

Gutell RR, Power A, Hertz GZ, Putz EJ, Stormo GD. 1992. Identifying constraints on the higher-order structure of RNA: Continued development and application of comparative sequence analysis methods. *Nucleic Acids Res 20*:5785–5795.

He L, Kierzek R, SantaLucia J Jr, Walter AE, Turner DH. 1991. Nearest neighbor parameters for GU mismatches: GU/UG is destabilizing in the context CGUG/GUGC UGUA/AUGA, and AGUU/UUGA but stabilizing in GGUC/CUGG. *Biochemistry 30*:11124–11132.

Heilman-Miller SL, Pan J, Thirumalai D, Woodson SA. 2000. Role of counterion condensation in the folding of the *Tetrahymena* ribosyme II. Counterion-dependence of folding kinetics. *J Mol Biol 309*:57–68.

Hermann T, Westhof E. 1998. Exploration of metal ion binding sites in RNA folds by Brownian-dynamics simulations. *Structure 6*: 1303–1314.

Jovine L, Djordjevic S, Rhodes D. 2000. The crystal structure of yeast phenylalanine tRNA at 2.0 Å resolution: Cleavage by Mg^{2+} in 15-year old crystals. *J Mol Biol 301*:401–414.

Kieft JS, Tinoco I Jr. 1997. Solution structure of a metal-binding site in the major groove of RNA complexed with cobalt (III) hexammine. *Structure 5*:713–721.

Laing LG, Gluick TC, Draper DE. 1994. Stabilization of RNA structure by Mg ions. *J Mol Biol 237*:577–587.

Leontis NB, Ghosh P, Moore PB. 1986. Effect of magnesium ion on the structure of the 5S RNA from *Escherichia coli*. An imino proton magnetic resonance study of the helix I, IV, and V regions of the molecule. *Biochemistry 25*:7386–7392.

Leontis NB, Westhof E. 1998. The 5S loop: Chemical probing and phylogenetic data versus crystal structure. *RNA 4*:1134–1153.

Leontis NB, Westhof E. 2001. Geometric nomenclature and classification of RNA base pairs. *RNA 7*:499–512.

Madura JD, Davis ME, Gilson MK, Wade RC, Luty BA, McCammon

JA. 1994. Biological applications of electrostatic calculations and Brownian dynamics simulations. *Rev Comput Chem 5*:229–267.
Manning GS. 1977. Limiting laws and counterion condensation in polyelectrolyte solutions. IV. The approach to the limit and the extraordinary stability of the charge fraction. *Biophys Chem 7*:95–102.
Masquida B, Westhof E. 1999. Crystallographic structures of RNA oligoribonucleotides and ribozymes. In: Neidle S., ed. *Oxford Handbook of Nucleic Acid Structure*, Oxford: Oxford University Press. pp 533–565.
Masquida B, Westhof E. 2000. On the wobble GU and related pairs. *RNA 6*:9–15.
Mathews DH, Sabina J, Zuker M, Turner DH. 1999. Expanded sequence dependence of thermodynamic parameters improves prediction of RNA secondary structure. *J Mol Biol 288*:911–940.
McDowell JA, He L, Chen X, Turner DH. 1997. Investigation of the structural basis for the thermodynamic stabilities of tandem GU wobble pairs: NMR of (rGGAGUUCC)2 and (rGGAUGUCC)2. *Biochemistry 36*:8030–8038.
McDowell JA, Turner DH. 1996. Investigation of the structural basis for thermodynamic stabilities of tandem GU mismatches: Solution structure of $(rGAGGUCUC)_2$ by two-dimensional NMR and simulated annealing. *Biochemistry 35*:14077–14089.
Misra VK, Draper DE. 1999a. On the role of magnesium ions in RNA stability. *Biopolymers 48*:113–135.
Misra VK, Draper DE. 1999b. The interpretation of Mg^{2+} binding isotherms for nucleic acids using Poisson–Boltzmann theory. *J Mol Biol 294*:1135–1147.
Misra VK, Draper DE. 2000. Mg^{2+} binding to tRNA revisited: The nonlinear Poisson–Boltzmann model. *J Mol Biol 299*:813–825.
Moore PB. 1999. Structural motifs in RNA. *Annu Rev Biochem 68*:287–300.
Porschke D. 1973. The dynamics of nucleic-acid single-strand conformation changes. Oligo- and polyriboadenylic acids. *Eur J Biochem 39*:117–126.
Pyle AM. 1993. Ribozymes: A distinct class of metalloenzymes. *Science 261*:709–714.
Record MT. 1975. Effects of Na^+ and Mg^{2+} ion on the helix-coil transition of DNA. *Biopolymers 14*:2137–2158.
Record MT, Lohman TM, de Haseth P. 1976. Ion effects on transitions of DNA and polynucleotides of variable linear charge density. *J Mol Biol 107*:145–158.
Richards EG. 1975. In: Fasman GD, ed. *Handbook of biochemistry and molecular biology: Nucleic acids*, 3rd ed. Cleveland, OH: CRC Press. p 197.
Romby P, Westhof E, Toukifimpa R, Mache R, Ebel JP, Ehresmann C, Ehresmann B. 1988. Higher order structure of chloroplastic 5S ribosomal RNA from spinach. *Biochemistry 27*:4721–4730.
Russell R, Millett IS, Doniach S, Herschlag D. 2000. Small angle X-ray scattering reveals a compact intermediate in RNA folding. *Nat Struct Biol 7*:367–370.
SantaLucia J Jr, Kierzek R, Turner DH. 1990. Effects of GA mismatches on the structure and thermodynamics of RNA internal loops. *Biochemistry 29*:8813–8819.
SantaLucia J Jr, Turner DH. 1993. Structure of (rGGCGAGCC)2 in solution from NMR and restrained molecular dynamics. *Biochemistry 32*:12612–12623.
Serra MJ, Axenson TJ, Turner DH. 1994. A model for the stabilities of RNA hairpins based on a study of the sequence dependence of stability for hairpins with six nucleotides. *Biochemistry 33*: 14289–14296.
Sharp KA, Friedman RA, Misra V, Hecht J, Honig B. 1995. Salt effects on polyelectrolyte-ligand binding: Comparison of Poisson–Boltzmann, and limiting law/counterion binding models. *Biopolymers 36*:245–262.
Shi H, Moore PB. 2000. The crystal structure of yeast phenylalanine tRNA at 1.93 Å resolution: A classic structure revisited. *RNA 6*:1091–1105.
Stein A, Crothers DM. 1976. Equilibrium binding of magnesium (II) by *Escherichia coli* tRNA-fMET. *Biochemistry 15*:157–160.
Szewczak AA, Moore PD. 1995. The sarcin/ricin loop, a modular RNA. *J Mol Biol 247*:81–98.
Tanner MA, Cech TR. 1996. Activity and thermostability of the small self-splicing group I intron in the pre-$tRNA^{Ile}$ of the purple bacterium *Azoarcus*. *RNA 2*:74–83.
Trikha J, Filman DJ, Hogle JM. 1999. Crystal structure of a 14 bp RNA duplex with non-symmetrical tandem G-U wobble base pairs. *Nucleic Acids Res 27*:1728–1739.
Williams AP, Longfellow CE, Freier SM, Kierzek R, Turner DH. 1989. Laser temperature-jump, spectroscopic, and thermodynamic study of salt effects on duplex formation by dGCATGC. *Biochemistry 28*:4283–4291.
Wimberly B, Varani G, Tinoco I Jr. 1993. The conformation of loop E of eukaryotic 5S ribosomal RNA. *Biochemistry 32*:1078–1087.
Woodson SA. 2000. Compact but disordered states of RNA. *Nat Struct Biol 7*:349–352.
Wu M, McDowell JA, Turner DH. 1995. A periodic table of symmetric tandem mismatches in RNA. *Biochemistry 34*:3204–3211.
Wu M, Turner DH. 1996. Solution structure of (rGCGGACGC)2 by two-dimensional NMR and the iterative relaxation matrix approach. *Biochemistry 35*:9677–9689.
Xia T, McDowell JA, Turner DH. 1997. Thermodynamics of nonsymmetrical tandem mismatches adjacent to G-C base pairs in RNA. *Biochemistry 36*:12486–12497.
Xia T, SantaLucia J Jr, Burkard ME, Kierzek R, Schroeder SJ, Jiao X, Cox C, Turner DH. 1998. Thermodynamic parameters for an expanded nearest-neighbor model for formation of RNA duplexes with Watson–Crick base pairs. *Biochemistry 37*:14719–14735.